J. Fluid Mech. (2013), *vol.* 729, *pp.* 584–602.
doi:10.1017/jfm.2013.330

Numerical calculations of two-dimensional large Prandtl number convection in a box

J. A. Whitehead[1,†], A. Cotel[2], S. Hart[3], C. Lithgow-Bertelloni[4] and W. Newsome[5]

[1]Physical Oceanography Department, Woods Hole Oceanographic Institution, Woods Hole, MA 02543, USA

[2]Civil and Environmental Engineering Department, University of Michigan, 1351 Beal Avenue, Ann Arbor, MI 48109, USA

[3]Geology and Geophysics Department, Woods Hole Oceanographic Institution, Woods Hole, MA 02543, USA

[4]Department of Earth Sciences, University College London, Gower Street, London WC1E 6BT, UK

[5]Geological Sciences Department, University of Michigan, 1100 North University Avenue, Ann Arbor, MI 48109, USA

(Received 30 August 2012; revised 17 June 2013; accepted 22 June 2013; first published online 24 July 2013)

Convection from an isolated heat source in a chamber has been previously studied numerically, experimentally and analytically. These have not covered long time spans for wide ranges of Rayleigh number Ra and Prandtl number Pr. Numerical calculations of constant viscosity convection partially fill the gap in the ranges $Ra = 10^3$–10^6 and $Pr = 1, 10, 100, 1000$ and ∞. Calculations begin with cold fluid everywhere and localized hot temperature at the centre of the bottom of a square two-dimensional chamber. For $Ra > 20\,000$, temperature increases above the hot bottom and forms a rising plume head. The head has small internal recirculation and minor outward conduction of heat during ascent. The head approaches the top, flattens, splits and the two remnants are swept to the sidewalls and diffused away. The maximum velocity and the top centre heat flux climb to maxima during head ascent and then adjust toward constant values. Two steady cells are separated by a vertical thermal conduit. This sequence is followed for every value of Pr number, although lower Pr convection lags in time. For $Ra < 20\,000$ there is no plume head, and no streamfunction and heat flux maxima with time. For sufficiently large Ra and all values of Pr, an oscillation develops at roughly $t = 0.2$, with the two cells alternately strengthening and weakening. This changes to a steady flow with two unequal cells that at roughly $t = 0.5$ develops a second oscillation.

Key words: buoyant boundary layers, convection in cavities, plumes/thermals

1. Introduction

Numerous laboratory experiments, numerical models and analytical studies have been used to investigate plumes of buoyant fluid rising up through an ambient fluid (e.g. Chay & Shlien 1986; Davaille & Jaupart 1993; Couliette & Loper 1995; Davaille

† Email address for correspondence: jwhitehead@whoi.edu

et al. 2011, and references therein). The limit of very viscous 'Stokes flow' has received much attention in efforts to improve knowledge about possible behaviour and structure of vertical thermally driven plumes within Earth's mantle (Schubert, Turcotte & Olson 2001; Suetsugu, Steinberger & Kogiso 2005). Starting with a motionless viscous fluid and a thinner layer of lighter fluid along the bottom, the bottom layer develops a gravitational Rayleigh–Taylor instability (Whitehead & Luther 1975) so that the low-density fluid accumulates in a large spherical blob that ascends to the surface. The spacing (wavelength) is determined by the kinematic viscosity ratio between the interior and the thinner layer fluids. Following that ascent, remnant light material continues to ascend from bottom to top in localized conduits. A steady injection of lighter fluid at the bottom of a layer of viscous fluid results in the ascent of a similar large blob of material. In addition, if the injected fluid is the same material with higher temperature than ambient fluid, the rising hot spherical body conducts heat outward and thereby incorporates additional host material into the plume head as it rises (Griffiths 1986). As the material arrives at a top horizontal surface, it spreads laterally (Olson & Singer 1985). If the fluid source at the bottom stays on, fluid from the conduit continues to feed fluid to the top. Numerical models more precisely quantify internal flow and temperature, even though additional features, such as the presence of bottom, top and lateral boundaries, or conditions more like the Earth's mantle, do not lead to any new changes to this sequence (Farnetani & Hofmann 2009; van Keken, Davaille & Vatteville 2009; Vatteville *et al.* 2009).

How does such a plume from a local source proceed to final steady flow? This question prompted our numerical study to calculate flow of a plume for extended periods of time compared to those in laboratory experiments and numerical work. Our layout is constructed so that calculations can be conducted over very long periods of time. The two-dimensional chamber has height equal to width. Convection is driven by elevated temperature ΔT along part of the bottom of this chamber starting from constant cold temperature. The same cold temperature is set elsewhere along the bottom and along the top. Conductive heat flow out of the sides is zero. The calculations continue for up to two thermal diffusive times. Only two relevant dimensionless numbers exist: the Rayleigh number Ra (a measure of the thermal forcing), and the Prandtl number Pr (the ratio of kinematic viscosity to thermal diffusivity). There are also two geometric numbers that are fixed in this study. The ratio of width to depth of the chamber has a value of 1 and the ratio of the size of the local hot region on the bottom to width is kept at 0.5. Although this is not the optimal geometry to compare with possible flows in the Earth's mantle, it is the simplest one for a starting point.

The objective of our project is to provide 'benchmark' cases for comparison with the many different flows that have been produced numerically and in the laboratory. These typically involve more complex fluids, larger chambers, and shorter periods of time than the two thermal time constant durations here. One question of particular interest is: 'Do existing laboratory experiments using fluids with Pr up to 10^4 behave like flow for infinite Pr?' Although we do not study a model of a plume in the Earth's mantle, flow with very large Pr is relevant to mantle studies in general since the mantle has a Pr of $\sim 10^{23}$.

We find that the flow continues to evolve over times of the order of the thermal diffusive time scale. Therefore, flows can be expected to take even longer to become steady for more complex geometries such as cases with wider layers, plumes in the presence of internal heating with strong sinking subduction zones, or for a spherical shell. All of these must be added to produce a model of the Earth's mantle.

Following the formulation in § 2, § 3 contains a description of flow at $Ra = 10^6$ and $Pr = \infty$. Surprisingly, this flow becomes periodic in time. Section 4 shows the increased complexity of flows with increasing Ra over the range $10^3 < Ra < 10^6$. Section 5 shows that the motion and temperature fields in the range $1 \leqslant Pr \leqslant \infty$ have the same form as for the infinite Pr case. However, flow with smaller Pr takes longer to develop because of inertia.

2. Formulation

The incompressible Boussinesq equations for this model in Cartesian coordinates express continuity, momentum, and energy conservation:

$$\boldsymbol{\nabla}' \cdot \boldsymbol{u}' = 0, \tag{2.1a}$$

$$\rho_0 \frac{\partial \boldsymbol{u}'}{\partial t'} + \rho_0 \left(\boldsymbol{u}' \cdot \boldsymbol{\nabla}'\right) \boldsymbol{u}' = -\boldsymbol{\nabla}' p' + \mu \nabla^2 \boldsymbol{u}' + g\alpha\rho_0 T \boldsymbol{k}, \tag{2.1b}$$

$$\frac{\partial T'}{\partial t'} + \boldsymbol{u}' \cdot \boldsymbol{\nabla}' T' = \kappa \nabla'^2 T', \tag{2.1c}$$

in which the velocity vector is $\boldsymbol{u}'$, density is ρ with the average density ρ_0, temperature is T', time is t', viscosity is μ, acceleration of gravity is g, the linear thermal coefficient of expansion is α, thermal diffusivity is κ, specific heat at constant pressure is C_p and $\boldsymbol{k}$ is a unit vector in the direction of gravity directed downward in the z' coordinate direction. The prime denotes dimensional variables of internal temperature, velocity and location. Initially the temperature everywhere is T_0. The fluid is in a two-dimensional box of size D. Temperature is T_0 along top and bottom except at a strip centred along the bottom, where it is suddenly raised to $T_0 + \Delta T$ at time $t = 0$.

The equations are made dimensionless using a velocity scale κ/D (a common scaling for cellular convection), temperature scale ΔT (dimensionless temperature is in deviation from T_0), and time scale D^2/κ, where $\kappa = k/\rho_0 C_p$ is thermal diffusivity, in which k is thermal conductivity. Henceforth all symbols are unprimed and dimensionless. The heat equation is

$$\frac{\partial T}{\partial t} + \boldsymbol{u} \cdot \boldsymbol{\nabla} T = \nabla^2 T. \tag{2.2a}$$

For two-dimensional Cartesian flow and constant viscosity, the equation for vorticity $\zeta = \partial w/\partial x - \partial u/\partial z$ is

$$\left(\frac{1}{\mathrm{Pr}}\left(\frac{\partial}{\partial t} + \boldsymbol{u} \cdot \boldsymbol{\nabla}\right) - \nabla^2\right) \zeta = -Ra \frac{\partial T}{\partial x}, \tag{2.2b}$$

and the equation for the streamfunction ψ, where $u = -\partial\psi/\partial z$ and $w = \partial\psi/\partial x$, is

$$\nabla^2 \psi = \zeta. \tag{2.2c}$$

The dimensionless numbers are $Ra = g\alpha\Delta T D^3/\kappa\nu$ and $Pr = \nu/\kappa$ (kinematic viscosity is $\nu = \mu/\rho_0$). Equation (2.2*a*) is advanced numerically using a standard leapfrog-trapezoidal scheme for each time step δt (Durran 1999). Then, (2.2*b*) is solved in one of two ways: either by a time advance for fixed values of Pr and Ra using the same leapfrog scheme or by using a standard MATLAB Poisson equation solver for infinite Pr. Then, to convert vorticity to the streamfunction, (2.2*c*) is solved using the MATLAB Poisson solver. The axis z is zero at the bottom and positive up, and x is zero on the left and positive to the right. Boundary conditions are set to $\psi = \zeta = 0$ (no volume flux and free-slip) for all x at $z = 0, 1$ and for all z

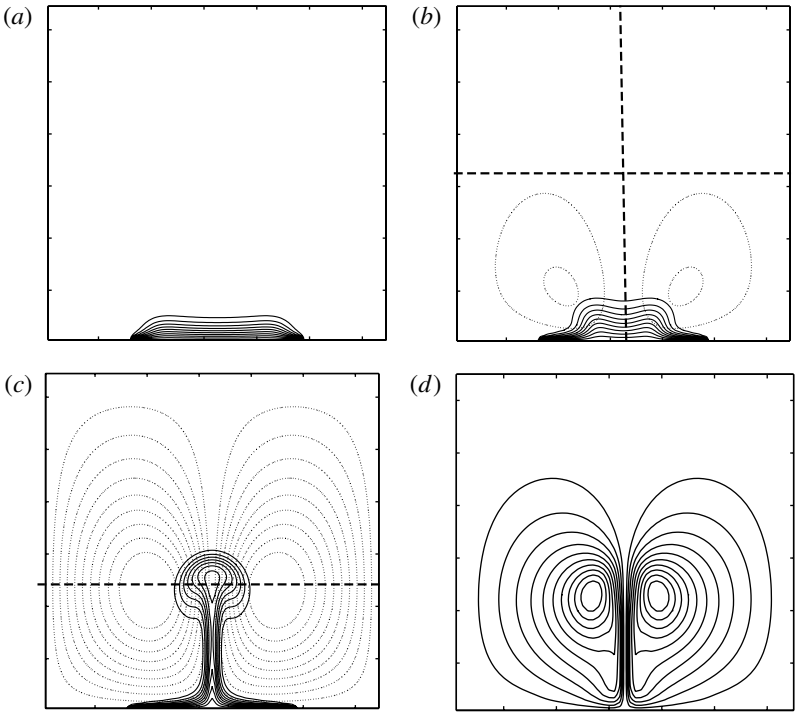

FIGURE 1. (*a–c*) Temperature (solid) and streamfunction ψ (dotted) contours, and (*d*) vorticity ζ when the thermal plume becomes established for $Ra = 10^6$ and $Pr = \infty$ (*d*) vorticity: (*a*) $t = 0.0006$, (*b*) $t = 0.0009$, (*c,d*) $t = 0.00124$ (when vorticity is greatest). Isotherm contours are every 0.1, streamfunction contours are every 20, and vorticity contours are every 2000. The horizontal dashed lines are profile locations for figure 4 and the vertical dashed line is the vertical profile location for figure 5.

at $x = 0, 1$ (the bottom, top and sidewalls of the square box). In addition, a zero normal temperature gradient (zero sideways heat conduction) is imposed, for all z at $x = 0, 1$, and $T = 0$ is set at $z = 0, 1$ except along a centred segment extending from $1/4 < x < 3/4$ along the bottom where $T = 1$. The initial conditions are $\psi = \zeta = T = 0$ in the interior.

3. Results for $Ra = 10^6$ and infinite $Pr = \infty$

3.1. *The symmetric cell*

We first show the flow and temperature evolution for $Ra = 10^6$ and $Pr = \infty$. The grid size is 128×128 and the numerical time step is 10^{-6}. Using these results, § 3.2 compares the same patterns using different grid sizes and time steps.

Initially, heat conducts up from the bottom (figure 1*a*). Two buoyancy-driven cells begin to focus the hot blob toward the centre (figure 1*b*). The instant $t = 0.00124$ (figure 1*c,d*) is significant because the greatest value of vorticity is generated. By that time, the plume head is fully established (figure 1*c,d*) with a thermal conduit below it.

Next, at $t = 0.0015$ (figure 2*a,b*) the head reaches the top of the tank and begins to flatten out. Note that even though the temperature pattern is complicated, the streamfunction pattern consists of two cells smoothly distributed throughout the chamber as expected for Stokes flow (figure 2*a,c,e*). When the plume head approaches

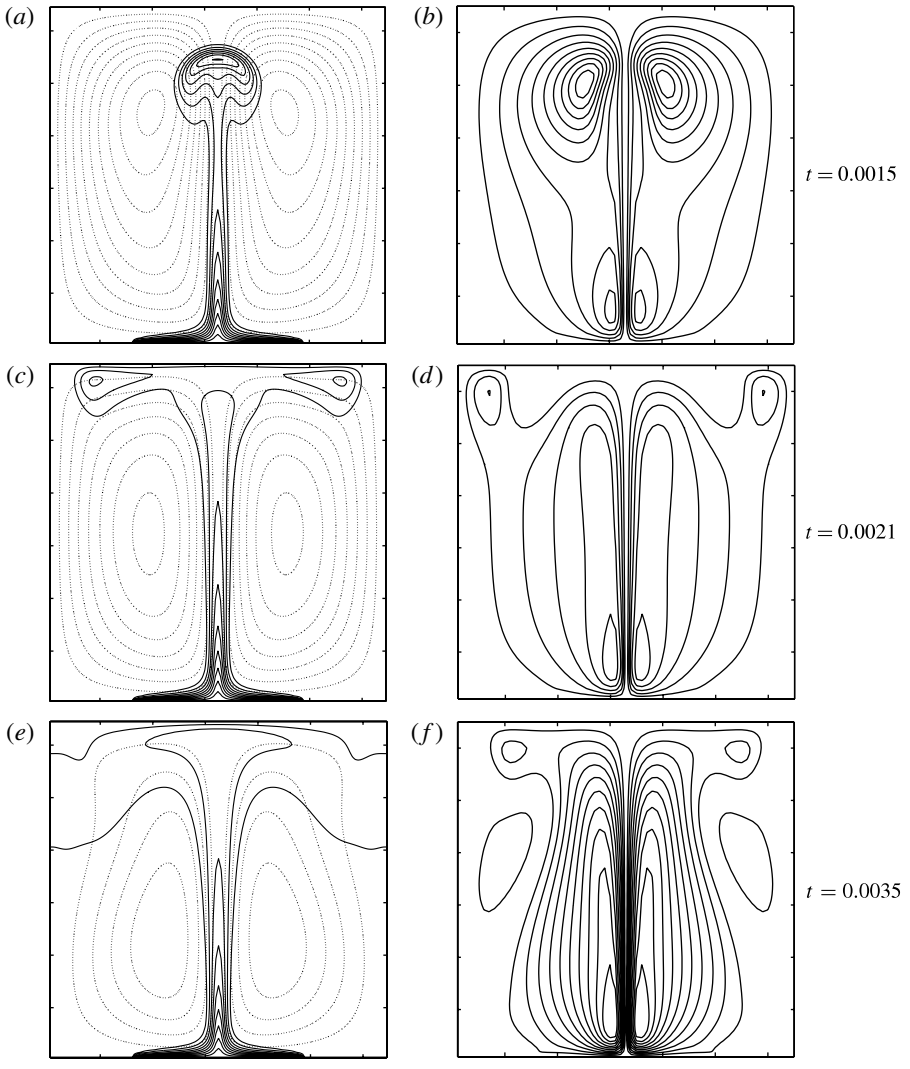

FIGURE 2. (*a,c,e*) Temperature (solid) and streamfunction ψ (dotted) and (*b,d,f*) vorticity at the times when the thermal plume ascends to the top (*a,b*), spreads out (*c,d*), and a balance between vorticity production from rising and sinking is established (*e,f*) for $Ra = 10^6$ and $Pr = \infty$: (*a,b*) $t = 0.0015$, (*c,d*) $t = 0.0021$, (*e,f*) $t = 0.0035$. Isotherms are every 0.1, streamfunction contours are every 20, and vorticity contours are every 2000 in (*b,d*) and every 1000 in (*f*).

the top, the vorticity has two pairs of extrema (figure 2*b*). The upper pair is next to the plume head and the lower pair is next to the conduit. As the plume head with hot material spreads out under the top lid, the top pair spreads laterally to the walls and the two pairs of extrema become almost equal in magnitude (figure 2*d,f*). After this, the flow field changes more slowly. The relatively steady flow at this stage has a hot conduit in the centre and cold boundary layers that slowly strengthen along both sidewalls. The interior temperature of the counter-rotating cells slowly changes from being isothermal at $T = 0$ (figures 1*c*, 2*a,c*) to isothermal at $T = 0.5$ through

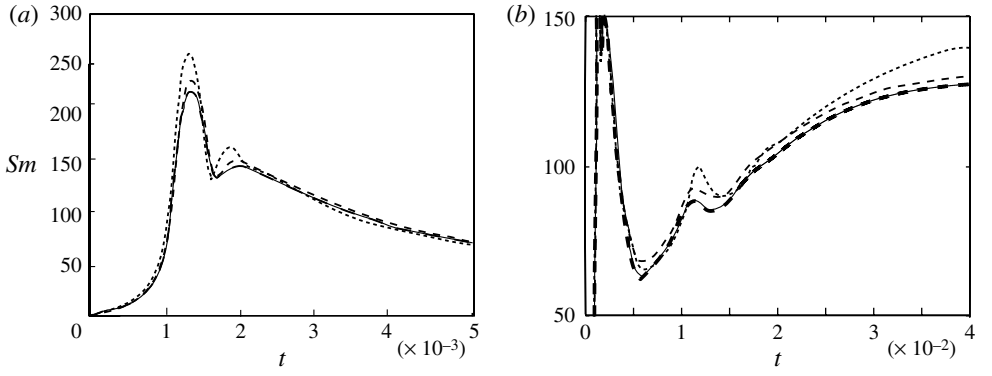

FIGURE 3. Calculations of *Sm* versus time for different grid sizes for $Ra = 10^6$ and $Pr = \infty$. (*a*) Early time, when the plume head arrives at the top and spreads out. (*b*) Time up to 0.04 with expanded resolution of *Sm*. Square grid sizes are: 32 (dots), 64 (short dashes), 128 (long heavy dashes) 256 (solid thin line).

plumes that wrap around the core. This is illustrated by the $T = 0.4$ isotherm that is still wrapping around at $t = 0.01$ (figure 2*e*). The flow approaches the well-known boundary layer solution for convection cells at large Rayleigh number (Schubert *et al.* 2001).

3.2. *Comparison of different grid sizes and time steps*

The evolution in § 3.1 happens with any grid size and time step giving stable calculations, but quantitative studies require specification of the grid size and time step needed for acceptable resolution. Here, we compare results with 32, 64, 128 and 256 square grids. The speed of the circulation is particularly useful to determine vigour of the convection. The velocity field itself is relatively smooth, but this speed is affected by the heat transported by bottom thermal boundary layer diffusion, which is strongly improved by smaller grid size, especially at the corner of the temperature profile along the bottom. Speed is quantified by calculating the maximum value of the streamfunction *Sm*, which is defined by

$$Sm(t) = \max\left(|\psi|\right)(t). \tag{3.1}$$

This is plotted as a function of time for calculations using the four grid sizes. At first, *Sm* increases with time (figure 3*a*) as the plume head forms. It takes a maximum value with the coarsest grid (32) having a maximum much greater than the rest. The maximum values of *Sm* for calculations with 64, 128 and 256 grids lie within 2 % of each other. After the plume head arrives at the top, there is a sudden and rapid decrease in *Sm* (figure 3*a,b*). Then, a period of slow change occurs as the temperature maxima in the two vortices are swept to the side and down near the walls. All the curves for different grid sizes are close to parallel, with the finer grid having slightly smaller *Sm*. At $t = 0.04$, the strength of *Sm* is still approaching a steady value that is smaller than the maximum value at earlier times. The 256 grid values are a maximum of 1.2 % different from the 128 grid values during the early time when the plume head rises and spreads out. The two curves overlap each other in figure 3(*b*) and are not distinguishable by eye. This difference is consistent with the fact that total heat flux into the system depends on grid size because of the temperature jump along the bottom.

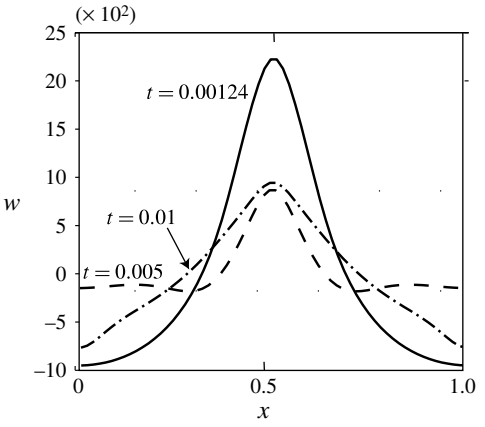

FIGURE 4. Horizontal profiles of vertical velocity across the tank for $Ra = 10^6$ and $Pr = \infty$ at three times. First, the instant of peak vorticity ($t = 0.00124$, profile location shown in figure 1*c*). Second, when the head has arrived at the top and spread out ($t = 0.005$). Third, when the head has been conducted away at $t = 0.01$. (The location of the latter two profiles is shown in figure 1*b*).

The vorticity maximum at time $t = 0.0024$ is also a useful diagnostic value for grid size. The value of the maximum for a 64 grid is ∼1.8 % higher than for a 128 grid, and that maximum is ∼0.6 % higher than the 256 grid. On the basis that a 256 grid produces only about a 0.6 % correction in vorticity maximum, and only a 1.2 % correction in *Sm*, all calculations for the figures and table 1 are made with a 128 × 128 grid, unless a different size is stated.

Time must be small enough to avoid any numerical instability, which is easily detected as either zigzagging contour plots or numerical collapse of the computation. For the 128 grid, a time step 5×10^{-6} produces some visible zigzags during the transient events up to $t = 0.04$, and a numerical collapse occurs for the larger time step 2×10^{-5}. Results in this paper use a time step of 10^{-6}. For comparison, a time step of 10^{-7} faithfully reproduces the track for the 128 grid shown in figure 3 except that the first peak is 1 % smaller, and there is a slight lag in time of the peak. Later, when the flow is becoming relatively steady at $t = 0.04$, the tracks for time steps of 10^{-6} and 10^{-7} overlap quite precisely, within one part in 4×10^{-6}.

3.3. *Profiles and trajectories*

At all times, the streamfunction ψ and the consequent flow field is smooth, as illustrated by profiles of vertical velocity w at two different levels and at three different times (figure 4). The solid curve is located at the depth that horizontally intersects the middle of the plume head at the moment of greatest overall vorticity (this depth is shown in figure 1*c*). The upward velocity is concentrated near the centre with a maximum velocity of ∼2250. The next profile at $t = 0.005$ is at mid-depth (location in figure 1*b*), where the top plume is spreading out. The peak velocity is ∼900, less than half the velocity during the ascent. After considerably more time ($t = 0.01$), the peak velocity of about 1000 is reached, which is slightly larger than the peak velocity at $t = 0.005$. By this time, the vertical motion at mid-depth exhibits almost constant shear.

As the plume head rises to the top, recirculation within the head is measured with Lagrangian trajectories of particles. The trajectories in figure 5 show the most dramatic

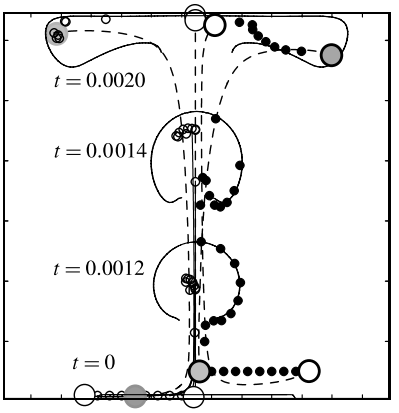

FIGURE 5. Particle trajectories starting on a line at elevation 0.0178 (left) and 0.14 (right) at four different times at $Ra = 10^6$ and $Pr = \infty$. The 0.1 isotherms are shown around the heads at the times indicated. Dashed lines indicate trajectories of particles that are indicated by larger circles and discussed in the text.

features during plume head formation and ascent at four different times. The outer extents of the heads are shown by contours of the 0.1 isotherm. This isotherm is not drawn in the region of the stem below the head to simplify the figure. Particles with a starting location very near (almost touching) the bottom (elevation = 0.0178) are shown on the left-hand side of figure 5. They are swept laterally into the head and ascend in a cluster within the head all the way to the top, rotating by $\sim 45^\circ$ during ascent. Then, they spread out horizontally in a region close to the top. The particle location at the final time depends strongly on each initial position. The particles starting in the middle of the initial line arrive near the outside of the spreading plume head (larger grey circle and many smaller open circles). In contrast, the particles starting at both edges of the initial line (larger white circles with narrow border) both arrive at the centre of the top. To the right of centre are particles (solid dots with two large circles) starting eight times higher above the bottom than the particles on the left (at elevation = 0.14). At $t = 0.0012$, these particles encircle the outer part of the plume head. They have been swept there during the formation of the plume head (figure 1*b*). At $t = 0.0014$, shear rearranges the particle pattern around the head. The pattern resembles a spiralling dye pattern observed by Griffiths (1986), and attributed to thermal entrainment. After the head spreads out under the top, the particles have rotated approximately 180° clockwise so that the particle that was initially outermost from the centre (white circle with black border) ends up close to the centre, and the particle that was initially close to the centre (grey circle with black border) finishes up near the side. Therefore, we have seen two examples of particle trajectories, one that folds and the other that rotates.

Vertical profiles of temperature at the exact centre show the ascending plume and then the slower subsequent adjustment (figure 6). First, the conductive profile forms at $t = 0.0006$ and 0.0009. We then see that, sequentially, the rising plume head is fully formed ($t = 0.00012$), the head has risen to near the top ($t = 0.0015$), and it spreads out ($t = 0.0021$ and 0.0035). Then, there is a slow change in the rising conduit profile, probably caused by the gradual change of temperature within the two cells.

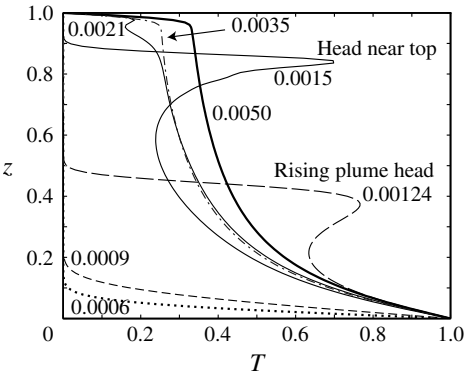

FIGURE 6. Vertical distribution of temperature in the middle of the chamber at various times (indicated near each curve) for $Ra = 10^6$ and $Pr = \infty$.

3.4. *Broken symmetry and oscillations*

As time continues to time $t = 2$ (figure 7), the trajectory of Sm approaches almost a constant value, but then two oscillations sequentially develop. At approximately $t = 0.16$ an oscillation is visible and it becomes relatively steady in size (figure 7*b,c*). The oscillation comes from a growing perturbation whose amplitude can be traced back in time all the way to the very tiny truncation amplitude. It violates mirror symmetry and consists of alternate strengthening and weakening of the two cells. It also has two frequency components, and at about $t = 0.36$ the primary period doubles. Then, a relatively complicated flow mixes the fluid, resulting in a steadier flow with two cells of unequal size. At about $t = 0.5$ the second oscillation appears. This oscillation initially also has two periods that are visible as a slow modulation of the peak-to peak amplitude (figure 7*e*). At about $t = 0.8$ it becomes an oscillation of single frequency and constant amplitude that continues to $t = 2$ (figure 7*f*). This is strictly periodic down to the truncation level with no other signal growing.

The numerical code has right–left symmetry down to the numerical truncation level of $O(10^{-16})$, which is a noise signal. A small growing disturbance is initiated by this noise. This is visible, for example, as a growing oscillation at the time $t = 0.115$ prior to the visible onset of the first oscillation (figure 7*b*). To determine whether this growing oscillation has exponential growth, note that the exponential growth of a signal from numerical noise to a size of $O(1)$ takes the time $t/\tau = \ln(10^{16}) \cong 36.8$. We assume that the characteristic growth time τ arises from the solution of a linear instability problem. No theory exists to give the value of τ, but the growing amplitude as seen in figure 7(*b*) (but with the slow trend in mean amplitude subtracted) is linear on a semi-log plot. This shows that the growth is exponential, and the measured value of the growth time is $\tau = 0.0054$.

The growing perturbation shown in figure 7(*c*) can be triggered earlier than at $t = 0.16$ by numerically imposing a disturbance larger than the noise. In that case, the oscillation appears sooner.

A time series of the vertical temperature gradient at the centre of the top boundary reveals the dimensionless conductive heat flux delivered by the convection. The heat flux is called HF and is defined by

$$HF\,(t) = N \times T(0.5, N - 1, t), \tag{3.2}$$

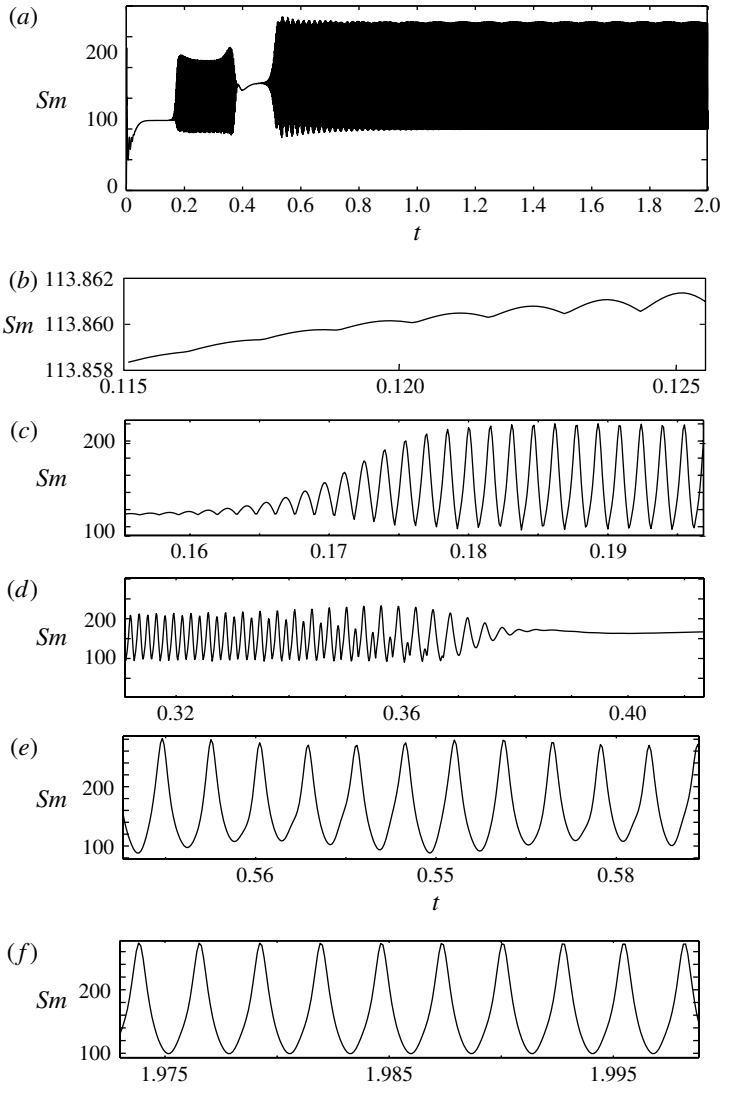

FIGURE 7. The evolution of Sm for different time intervals for $Ra = 10^6$ and $Pr = \infty$. (*a*) Over the first 2 time units. (*b*) A growing very small disturbance. (*c*) Growth of the first oscillation. (*d*) Two cells of uneven size and decay of the first oscillation. (*e*) The second oscillation after its start. Note the amplitude vacillation. (*f*) The final steady oscillation.

where N is the number of vertical levels starting from the bottom. The scaling used here dictated that dimensionless heat flow for the conductive state is 1. Therefore, HF is equivalent to the Nusselt number Nu. However, we will only refer to Nu in the context of average heat flow, that is to say, (3.2) averaged over some time span.

Time series of HF with two different grid sizes are shown in figure 8. The approximate shape of the two series is similar, but the oscillation transition time with the finer grid resolution occurs a little later. Closer inspection of the series (not shown) reveals that even the shapes of the curves during transition overlie each other. The value of the oscillation amplitude of HF is about three per cent smaller for the

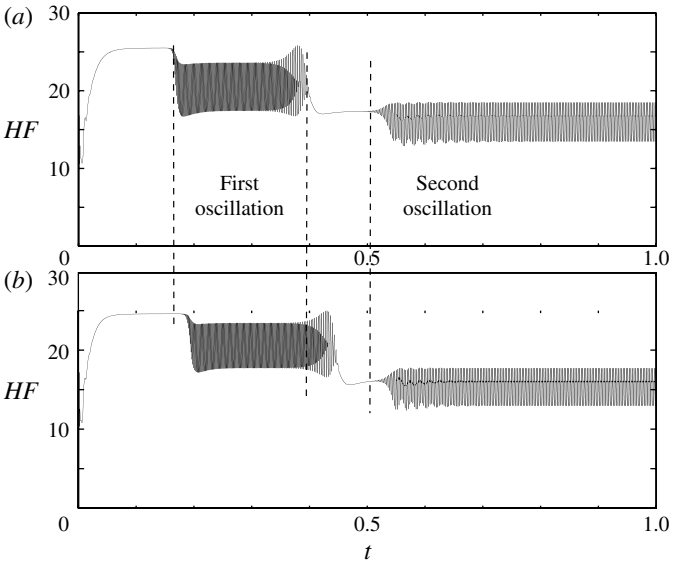

FIGURE 8. *HF* versus time for $Ra = 10^6$ and $Pr = \infty$ and two different grid sizes (*a*) 64×64, (*b*) 128×128.

128 grid than for the 64 grid. This is consistent with better resolution with a finer grid of the derivative at the boundary.

Figure 8 shows one other important aspect. Recall that there are four successive flow types: steady flow with two cells of the same size, the first oscillation, slowly changing flow with two cells of unequal size, and the second oscillation. Figure 8 shows that *Nu* becomes lower for each successive flow type. The dynamical reason for this is unclear.

The oscillations have simple structure. The first oscillation is a cyclic deflection of the conduit to the right and left, accompanied by strengthening of one cell and weakening of the other (figure 9). The descending cold conduits at the two sides alternately strengthen and weaken during the oscillation. Since both the right and left cells alternately become the strongest, the time series for *Sm* during much of the first oscillation has two peaks for each cycle. Therefore, the apparent period from figure 7(*c*) is half the period illustrated in figure 9.

A gradual change in size of both cells occurs during the first oscillation, with one cell slowly becoming larger than the other. Lagrangian material exchange is possible with two oscillating cells but not for steady flows, leading to volume exchange between the two cells. Near the end of the first oscillation, *Sm* from only the stronger cell dominates the time series, and since that oscillates only once per cycle, the period doubles in the record shown in figure 7(*c*). After the first oscillation ends, the flow has cells with two different sizes. Slowly thereafter, the second oscillation grows from small amplitude with two cells of different size. After it becomes large enough to see, the structure of the second oscillation is similar to that for the first oscillation with a speeding up and slowing down of the circulation (figure 10, visible as a change in the number of contours with time). Initially it possesses a slow modulation of the amplitude (figures 7*e*,*f*, 8) but the modulation vanishes at approximately $t = 0.8$.

Ra	*Ams*1	*Amf* 1	*Af* 1	*T*11	*T*12	*Ams*2	*Amf* 2	*Af* 2	*T*2
1000	0.30								
1750	0.58								
1800	0.60								
1825	0.61					2.39			
1875	0.63					2.54			
2000	0.68					2.89			
2125	0.74					3.21			
2500	0.92					4.04			
5000	2.45					7.91			
6250	3.21					9.40			
6875	3.56					10.08			
7200	3.74					10.43			
7238	3.76								
7275	3.78								
7350	3.83								
7500	3.91								
10^4	5.14								
2.5×10^4	10.46								
5×10^4	16.67								
5.63×10^4	18.00								
5.8×10^4	18.37								
5.94×10^4	18.64					26.43			
6.25×10^4	19.28					27.57			
7.5×10^4	21.70					31.80			
10^5	26.13					39.41			
2×10^5	40.77					63.08			
3×10^5	52.84					81.94			
4×10^5	63.50					98.30			
5×10^5	73.21					113.1			
5.25×10^5	75.52					116.6			
5.38×10^5	76.67	Brief	Brief	0.00213	0.00435	118.3			
5.5×10^5	77.80	92.35	36.9	0.00208	0.0043	120.2			
6×10^5	82.24	99.75	46.75	0.00201	0.00409	126.7			
7×10^5	90.71	114.3	66.05	0.00185	0.00374	139.9	141.5	67.3	0.00320
8×10^5	98.78	128.3	82.60	0.00172	0.00348	151.8	157.0	107.2	0.00300
9×10^5	106.5	140.7	101.2	0.00161	0.00325	163.2	172.0	140.3	0.00282
10^6	113.9	152.5	115.0	0.00152	0.00305	173.5	185.8	169.5	0.00269

TABLE 1. Amplitudes and frequencies of *Sm* for $Pr = \infty$. *T*11 is the period during the early stages of the first oscillation in the time interval when the amplitude is reasonably well defined and becoming steady (figure 7*c*). *Ams*1 is the time average of *Sm*. *Amf* 1 is the amplitude halfway between the peaks of the cycle and *Af* 1 is amplitude of the oscillation (peak to peak). This evolves and finally gives way to cyclic flow with roughly twice the period *T*12 (figure 7*d*). *Ams*2 is the (relatively) steady value of *Sm* between the two oscillations (also in figure 7*d*) or the time average if an oscillation is present. *Amf* 2 is the amplitude halfway between the peaks of the second oscillation cycle, and *Af* 2 is amplitude of the oscillation (peak to peak). *T*2 is the period of the second oscillation (figure 7*e*).

4. Results for $10^3 < Ra < 10^6$

Sequential runs over time, for many values of *Ra*, starting from $Ra = 1000$ reveal the successive emergence of many of the features described in § 3. To quantify these results, the amplitudes of symmetric or asymmetric, and steady or oscillating flows and

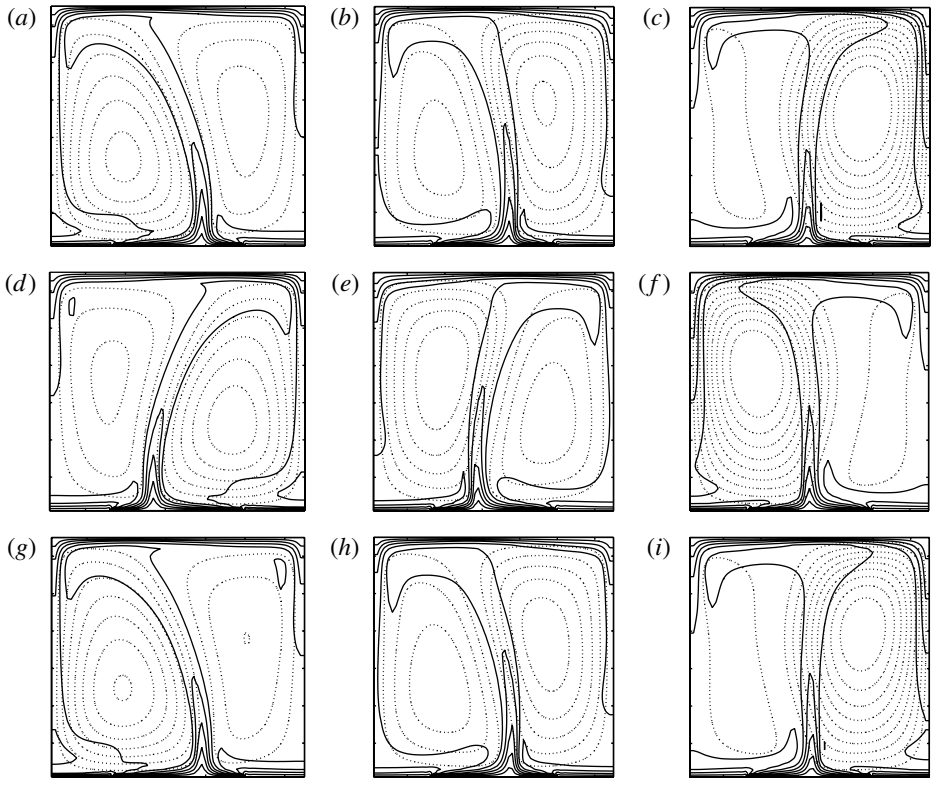

FIGURE 9. Temperature (solid) and streamfunction (dotted) for the first oscillation, for $Ra = 10^6$ and $Pr = \infty$: (*a*) $t = 0.1805$, (*b*) $t = 0.1810$, (*c*) $t = 0.1815$, (*d*) $t = 0.1820$, (*e*) $t = 0.1825$, (*f*) $t = 0.1830$, (*g*) $t = 0.1835$, (*h*) $t = 0.1840$, (*i*) $t = 0.1845$. Shown are every 0.1 isotherm and every 20 streamfunction contours.

the frequencies of any oscillations are taken from plots for *Sm* versus time. The results are listed in table 1.

Starting at $Ra = 1000$ there is no plume head during the formation period in the temperature field and no peaks with time in either *Sm* or *HF*. The flow and temperature field is right–left symmetric and there is no oscillation. At $Ra = 1825$, there is a transition to a flow that is off-centre with one large and one small cell producing an asymmetric temperature field. This is most easily triggered by a non-symmetric perturbation after the symmetric flow becomes steady. This perturbation is not absolutely necessary, however. If one waits long enough, the background numerical noise produces the transition, but the growth is so slow that the transition does not occur by $t = 2$.

Before continuing the description of the sequences in table 1, the flow at $Ra = 6000$ is shown if some detail (figure 11) because it illustrates the typical behaviour for low *Ra*. After a run begins, the flow and temperature fields approach values that appear to be steady (figure 11*a,b*). At a time depending upon the type of perturbation imposed on the flow, the flow is changes to the asymmetric flow (figure 11*c*). The transient plume during both the start of the original plume and during transition to the unsymmetric one produces a peak in the value of *Sm* (figure 11*d*). This peak is found

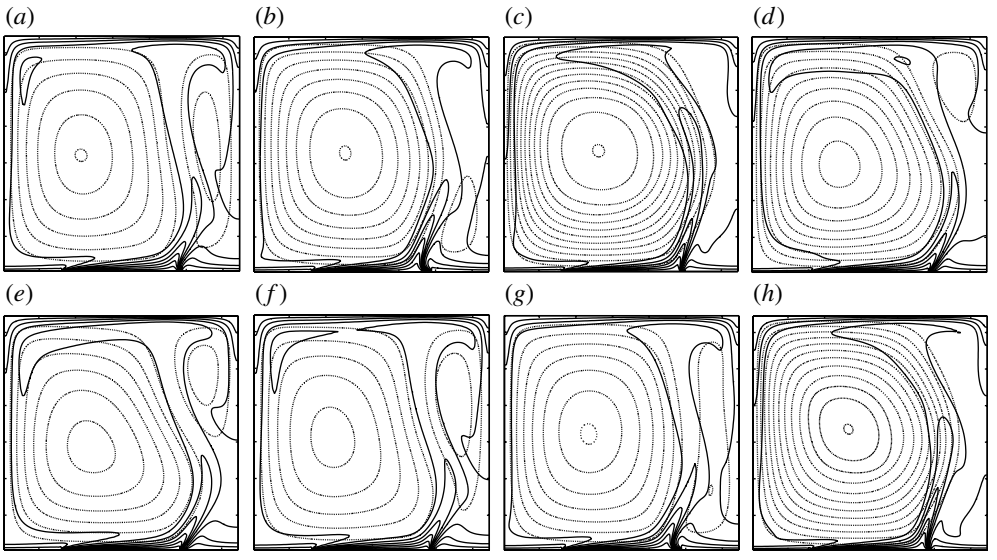

FIGURE 10. Temperature (solid) and streamfunction (dotted) for the second oscillation, for $Ra = 10^6$ and $Pr = \infty$: (*a*) $t = 1.0035$, (*b*) $t = 1.0040$, (*c*) $t = 1.0045$, (*d*) $t = 1.0050$, (*e*) $t = 1.0055$, (*f*) $t = 1.0060$, (*g*) $t = 1.0065$, (*h*) $t = 1.0070$. Shown are every 0.1 isotherm and every 20 streamfunction contours.

in the range $6000 \leqslant Ra \leqslant 1.1 \times 10^4$ but there is no accompanying peak in *HF*. Then, for $Ra > 11\,000 \pm 550$ there is a peak in *HF* during initial plume setup too.

Continuing with the sequence shown in the table 1, for $Ra < 1812.5 \pm 12.5$ the flow remains symmetric and steady and we have mentioned that there is no peak in *HF or Sm*. At $Ra = 1825$ the flow begins as a symmetric flow, but it changes to a non-symmetric steady flow. This transition continues until the run with $Ra = 7200$. In the range $7238 \pm 18 < Ra < 5.8 \times 10^4 \pm 6500$ the transition does not occur and a triggered perturbation decays with time, leaving the symmetric steady flow in place. Then the unsymmetric flow reappears at $Ra = 5.94 \times 10^4$. The first oscillation is found during the transition from the symmetric to the non-symmetric steady flow in the range $5.315 \times 10^5 \pm 6000 < Ra < 6.5 \times 10^5 \pm 4 \times 10^4$. Above the top value, and up to $Ra = 10^6$, both the first and second oscillations are found. The period of any of the oscillations lies within the circulation time, which, since each cell has approximately a width of $1/4$, is roughly equal to $1/4Sm$.

5. Effects of varying *Pr*

A finite value of *Pr* adds inertia to the momentum equations and, of course, inertia is relatively larger for smaller *Pr*. That means that as the thermal pattern rises into the interior from the bottom, the circulation must accelerate toward the exact balance between buoyancy and friction that inherently exists for infinite *Pr*. Although it is tempting to picture finite *Pr* effects as arising for smaller viscosity, it seems better to picture in one's mind that the circulation sets up more slowly with smaller *Pr*. There is smaller acceleration because of the larger inertia. Results for the time interval shown in figures 1 and 2 for $Ra = 10^6$ at four values of *Pr* plus the infinite *Pr* case (figure 12) dramatically show the sluggish nature of lower *Pr* flow along with

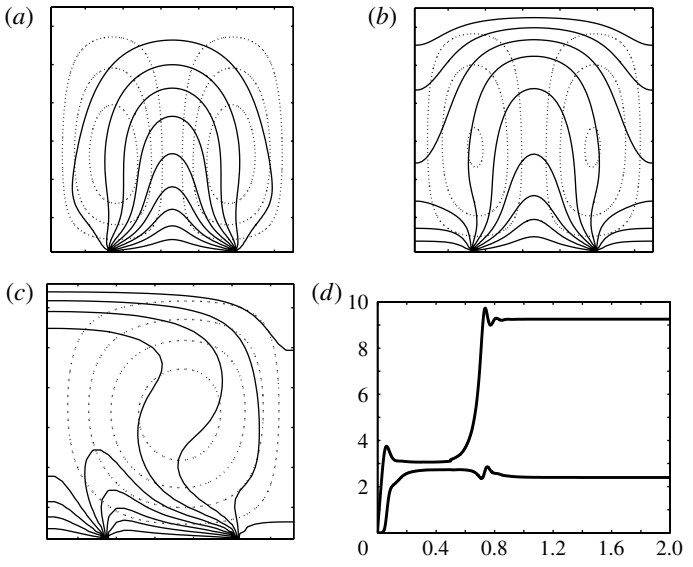

FIGURE 11. Results for $Ra = 6000$. (*a–c*) The temperature and streamfunction fields at different times. (*a,b*) Times $t = 0.06$ (*a*) and $t = 0.3$ (*b*). Isotherms are plotted for every 0.1 and streamfunction contours for every 1. (*c*) Time $t = 0.6$. A perturbation $T(0.2, 0.5) = 1$ was imposed on one grid point, and the flow changed to the non-symmetric flow shown here at $t = 2.0$. Streamfunction contours are plotted for every 2. (*d*) *Sm* and *HF* versus time.

a number of other features. First, the results for $Pr = 1000$ and infinity are identical to the eye throughout the entire sequence. Second, the formation of the plume head is slower for smaller *Pr*. Third, the form of the plume head is somewhat different for smaller *Pr*, with vorticity more concentrated at the side of the plume head resulting in the two vortices of opposite sign being further apart. The plume head rises a little faster than the two vortices. This leads to greater dipole separation as the head ascends to the top. For example, the dipole in the plume head for $Pr = 1$ at $t = 0.0050$ is further apart than the dipole for larger *Pr*. Although there is only small recirculation in the plume head and the vertical velocity near the head does not completely reverse in sign, parts of the plume rise more rapidly than others, and so there is a small amount of recirculation in the wake far away from the head itself. Such flows might be productively studied further. Fourth, as time gets to ~ 0.01 the flow begins to settle to steady flow and the effects of *Pr* are beginning to be small. For example, the flows for $Pr = 100$ and 1000 are almost identical to the infinite one. By $t = 0.1$ (not shown) flows with all *Pr* are almost identical.

Examination of the streamfunction peaks for different value of *Pr* gives insight into the effects of *Pr*. First, the peaks are very similar for both $Pr = 1000$ and infinity (figure 13). Second, for infinite *Pr* the peak in heat flux with time is present only for $Ra > 11\,000$, ($\pm 5\,\%$) and the peak in streamfunction is present only for $Ra > 6000$. For comparison, runs with $Pr = 1$ have a peak in heat flux only for $Ra > 9500$, and a peak in streamfunction only for $Ra > 5500$. Since these corresponding values are not too different, it is safe to conclude that the transition to flows with peaks is only weakly dependent on *Pr*.

The oscillations reported in § 3 are also present with finite *Pr*, and the basic behaviour appears to be the same as for infinite *Pr*. As *Ra* is increased from a

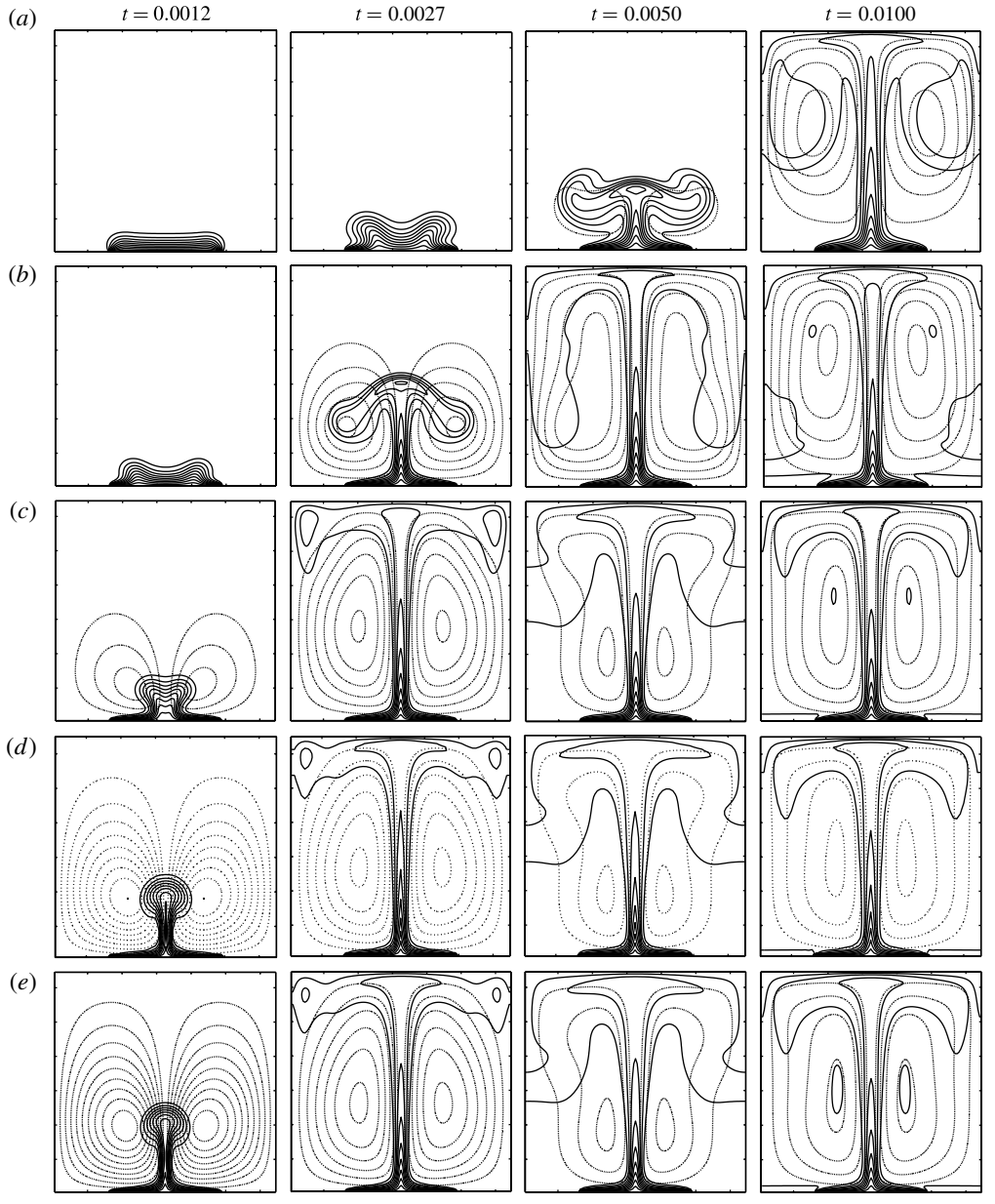

FIGURE 12. Sections of isotherms and streamfunction contours for runs with $Ra = 10^6$ at times $t = 0.0012$, 0.0027, 0.0050 and 0.0100 (left to right) for values of (*a*) $Pr = 1$, (*b*) $Pr = 10$, (*c*) $Pr = 100$, (*d*) $Pr = 1000$ and (*e*) $Pr = \infty$. Isotherms are every 0.1 and streamfunction contours are every 20.

value with steady flow, the oscillation onset seems to be relatively sluggish compared to infinite Pr and the oscillation period is longer. A quantitative study of oscillation amplitude and frequency versus Ra and Pr is not complete.

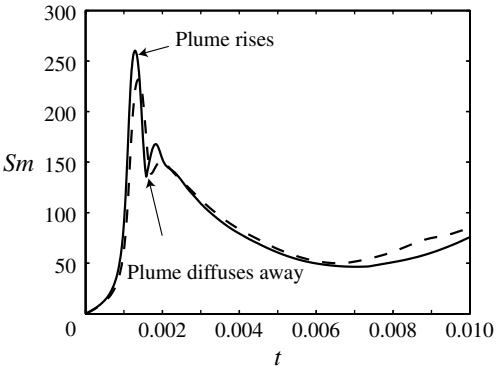

FIGURE 13. Evolution of Sm for $Ra = 10^6$ for $Pr = \infty$ (solid) and $Pr = 1000$ (dashed) as the plume head forms, rises, and spreads out along the top.

6. Discussion and summary

There are many estimates of the time required for deep plume formation and ascent in the Earth's mantle. Although our model is very simplified with constant viscosity, two dimensions, a square cross-section, only one width for the hot bottom, and free-slip sidewalls, these estimates of response time and velocities are still useful to inspect, even though the numbers would change with different geometrical parameters. A depth of 3000 km, and thermal conductivity of $\kappa = 10^{-6}$ m^2 s^{-1} yields a thermal diffusive time scale d^2/κ of 285 billion years (By). For $Ra = 10^6$ and $Pr = \infty$, the initial plume formation in figure 1 takes $\sim$0.001, which is equal to 285 million years (My). Estimating that the initial layer thickness follows $\sqrt{t}$, this gives a local value $Ra = 31.6$ at onset of motion. The error function solution for thickness at this time is smaller than the measured thickness in figure 1 due to small motions that the fluid has already developed at this time. Thus, the onset of motion here does not support a common assumption that the localized value of Ra is approximately 10^3 and close to critical (Schubert *et al.* 2001), a result supported by experimental observations and theory (Chay & Shlien 1986; Davaille & Jaupart 1993; Couliette & Loper 1995; Davaille *et al.* 2011) for convection over a uniformly heated bottom. Since the plumes studied here are from localized temperature, they apparently grow more quickly than plumes from smoother bottom temperature. Dimensionless time to rise to the top (figure 2) is 0.0004 units or 114 My and rise time for a particle of upwelling material following the plume head within the stem is about twice that or 228 My. It is not a surprise that these are somewhat longer than Earth values estimated from plume velocities in chambers that are very much greater than plume head diameter, e.g. 15–28 My (Richards, Duncan & Courtillot 1989).

Although some Rayleigh–Bénard laboratory experiments show independence of Pr for the emergence of oscillations (Krishnamurti 1970), other studies (Busse 1972; Busse & Whitehead 1974) associate such oscillations only to finite Pr effects so they incorporate the acceleration terms in the Navier–Stokes equations. The question of whether uniform viscosity convection at extremely large Pr, such as in the mantle of the Earth, can oscillate has remained open. Our results clearly show oscillations with truly infinite Pr, at least over a localized bottom temperature source in a box. Therefore, the first and second oscillations (figures 7–10) might exist in the mantle since finite amplitude effects can trigger them. The periods given in table 1, ranging

from 0.00152 to 0.00435 time scale units, (=0.433 to 1.2 By) are shorter than the Earth's age. Therefore, further studies with larger Ra and other geometries would clarify whether the new oscillations seen here are relevant for the Earth.

To summarize our results, there is a transient plume head for $Ra > 6000$–$11\,000$ consisting of a blob of hot fluid swept upward by a smooth velocity field. It has a small amount of internal circulation and it conducts relatively little heat outward during the rise from bottom to top except for the range $6000 < Ra < 11\,000$. These results verify results for axisymmetric flow by Griffiths (1986) with the absence of a plume head and no recirculation at small Ra. The material following the plume upward does not flow into the head as it does in transient turbulent high Reynolds number plumes (Turner 1962) and in injected experiments with large viscosity variation (Whitehead & Luther 1975; Griffiths & Campbell 1990). The head flattens and is dissipated away upon contact with the top lid as in Olson & Singer (1985) and then a steady thermal conduit conveys fluid up from the bottom to the top at the centre of the cell (Farnetani & Hofmann 2009; van Keken *et al.* 2009). For large Ra, both the top central heat flux HF and streamfunction Sm plotted with time have a distinct maximum as the plume rises and spreads out and then HF and Sm approach steady values. This sequence agrees with numerical calculations of the evolution of cellular convection for $Ra = 10^6$, $Pr = 7$ and 20 in a box three times wider than the depth (Hier-Majumder *et al.* 2002). In contrast to that study, our calculations produce no velocity boundary layer. In addition, our oscillation of the flow is not found in other studies over shorter periods of time or with different chamber sizes. The oscillating flow changes to a steady flow and then a second oscillation emerges. Previous experiments that report oscillations in high Pr convection by Krishnamurti 1970 and Busse and Whitehead 1974 might be related, but those experimental geometries differ significantly from ours.

These studies provide evidence that laboratory experiments with $Pr = 1000$ can be expected to have behaviour very close to the infinite case. Even for $Pr = 100$, the flow and temperature only vary by up to 3 % from infinite Pr convection. The largest effect of Pr is that small Pr convection has temperature and velocity lagging in time compared to larger Pr during the early transient portions of the flow. After that, the lag vanishes and the flow is independent of Pr. The balance between buoyancy and friction shown by (2.2*b*) is established even for the oscillations.

The results suggest a number of possible new directions. First, the oscillations have apparently not been analytically or experimentally investigated yet. Second, these calculations do not seem to approach the similarity solutions involving velocity boundary layers that are so well known for plumes, thermals, and conduits in semi-infinite regions (Turner 1962; Vatteville *et al.* 2009). A project to reconcile such calculations and similarity solutions would be useful. Third, we have calculated all the essential results using only a grid of 64×64 and a time step of 10^{-5} (although the results presented here used a 128×128 grid and time step of 10^{-6}). Such calculations have less precision, but they are much faster computations that are useful for student projects and educational demonstrations.

Acknowledgement

Support from the National Science Foundation was received under grants EAR-0551991 and EAR-0551999.

REFERENCES

BUSSE, F. H. 1972 The oscillatory instability of convection rolls in a low Prandtl number fluid. *J. Fluid Mech.* **52**, 97–112.

BUSSE, F. H. & WHITEHEAD, J. A. 1974 Oscillatory and collective instabilities in large Prandtl number convection. *J. Fluid Mech.* **66**, 67–80.

CHAY, A. & SHLIEN, D. J. 1986 Scalar field measurements of a laminar starting plume cap using digital processing of interferograms. *Phys. Fluids* **2**, 2358–2366.

COULIETTE, D. L. & LOPER, D. E. 1995 Experimental, numerical, and analytical models of mantle starting plumes. *Phys. Earth Planet. Inter.* **92**, 143–167.

DAVAILLE, A. & JAUPART, C. 1993 Transient high-Rayleigh number thermal convection with large viscosity variations. *J. Fluid Mech.* **253**, 141–166.

DAVAILLE, A., LIMARE, A., TOUITOU, F., KUMAGAI, I. & VATTEVILLE, J. 2011 Anatomy of a starting plume at high Prandtl number. *Exp. Fluids* **50**, 285–300.

DURRAN, D. R. 1999 *Numerical Methods for Wave Equations in Geophysical Fluid Dynamics*. Springer.

FARNETANI, C. G. & HOFMANN, A. W 2009 Dynamics and internal structure of a lower mantle plume conduit. *Earth Planet. Sci. Lett.* **282**, 314–322.

GRIFFITHS, R. W. 1986 Thermals in extremely viscous fluids, including the effects of temperature-dependent viscosity. *J. Fluid Mech.* **66**, 115–138.

GRIFFITHS, R. W. & CAMPBELL, I. H. 1990 Stirring and structure in mantle starting plumes. *Earth Planet. Sci. Lett.* **99**, 66–78.

VAN KEKEN, P. E., DAVAILLE, A. & VATTEVILLE, J. 2009 Dynamics of a laminar plume in a cavity: the influence of boundaries on the steady-state stem structure. *Geochem. Geophys. Geosyst.* **14**, 1–21.

KRISHNAMURTI, R 1970 On the transition to turbulent convection. Part 2. The transition to time-dependent flow. *J. Fluid Mech.* **42**, 309–320.

HIER-MAJUMDER, C. A., YUEN, D. A., SEVRE, E. O., BOGGS, J. M. & BERGERON, S. Y. 2002 Finite Prandtl number 2-D convection at high Rayleigh numbers. *Electron. Geosci.* **7**, 11–30; *Visual Geosci.* **2**, 1–53.

OLSON, P. & SINGER, H. 1985 Creeping plumes. *J. Fluid Mech.* **158**, 509–529.

RICHARDS, M. A., DUNCAN, R. A. & COURTILLOT, V. E. 1989 Flood basalts and hot-spot tracks: plume heads and tails. *Science* **246**, 103–107.

SCHUBERT, G., TURCOTTE, D. L. & OLSON, P. 2001 *Mantle Convection in the Earth and Planets*. Cambridge University Press.

SUETSUGU, D., STEINBERGER, B. & KOGISO, T. 2005 Mantle plumes and hot spots. In *Encyclopedia of Geology*, pp. 335–343. Elsevier.

TURNER, J. S. 1962 The starting plume in neutral surroundings. *J. Fluid Mech.* **13**, 356–368.

VATTEVILLE, J., VAN KEKEN, P., LIMARE, A. & DAVAILLE, A. 2009 Starting laminar plumes: comparison of laboratory and numerical modelling. *Geochem. Geophys. Geosyst.* **10**, Q12013.

WHITEHEAD, J. A. & LUTHER, D. S. 1975 Dynamics of laboratory diapir and plume models. *J. Geophys. Res.* **80**, 705–717.